

## ARTICLE INFO

Keywords:

## ABSTRACT

Here goes the abstract

## 1. Introduction

According to the International Renewable Energy Agency (IRENA) and the International Energy Agency (IEA), renewable energy sources (RES) are projected to account for at least 70% of global electricity generation by 2050 [1, p. 267]; [2, p. 20]. The increased penetration of renewable energy sources such as wind and solar is clearly demonstrated by the rapid growth of inverter-based resources; for example, by 2023, the global installed capacity of solar power generation alone had already exceeded that of the total installed hydropower capacity [3, p. 18 and 33]. This trend highlights the critical importance of researching grid converters to effectively integrate these energy resources into the power grid. Operating primarily as controlled current sources [4, p. 3-4], these converters are designed to ensure efficient power injection, comply with low-voltage ride-through (LVRT) requirements, and potentially provide ancillary services such as dynamic voltage support and frequency regulation [5, p. 5-6]. Despite their advantages, grid-connected converters face significant challenges in offering dynamic grid support under fault and disturbance conditions, emphasizing the necessity for advanced control strategies and optimized design methodologies to maximize efficiency [6, p.3-8], [7, p. 9-18].

Once connected to the grid, these converters are exposed to voltage sags, which are prevalent disturbances in power systems and are among the most frequently reported short-duration power quality issues worldwide [8, p. 12, 15, 22], [9]. To mitigate these effects, grid converters must remain connected and provide positive-sequence reactive current injection (RCI) to stabilize voltage conditions at the point of common coupling (PCC), as required by grid codes [10, p. 43-44], [11, p. 3, 5-6, 10, 18-19, 29-31]. This compensation introduces significant fluctuations in active ( $\bar{p}$ ) and reactive ( $\bar{q}$ ) power - typically twice the frequency of the grid - that can propagate through the network [12, p. 3-4, 6-7]. Likewise, these unbalanced conditions induce voltage oscillations in

the DC-link of grid-connected converters, resulting in significant capacitor ripple that exacerbates thermal stress, accelerates capacitor degradation, and ultimately reduces both reliability and component lifespan [13].



Since the early 2000s, various techniques have been proposed to address power control in grid-connected converters during voltage sags. Among them, Instantaneous Active-Reactive Control (IARC) has been widely recognized as the primary non-sinusoidal control strategy, as it inherently eliminates active and reactive power oscillations at the cost of high harmonic content current [15]. In contrast, five classical [16] sinusoidal current control strategies have been systematically analyzed in [17, 18, 19, 20]. These strategies are derived from different combinations of two coefficients,  $k_p$  and  $k_q$ , when imposed to assume discrete values of -1, 0, or 1 in the negative sequence voltage components of the reference current vector. Nonetheless, novel approaches that incorporate sophisticated techniques, such as model predictive control (MPC) [21] and sliding mode control (SMC) [22], have demonstrated improved dynamic response and LVRT capability. Additionally, emerging data-driven strategies, including intelligent adaptive power compensation [23] and fuzzy logic controllers [24] designed to enhance system resilience against grid disturbances, have gained attention. Although these new control paradigms may offer better performance, they generally entail a significantly higher computational cost and design complexity.

This paper aims to provide a thorough experimental quantification of the second harmonic component in power, introduced by the aforementioned classical sinusoidal current strategies, through frequency analysis under both lightly and heavily unbalanced conditions. Furthermore, key active and reactive power set-points are examined to assess the theoretical conditions for oscillation cancellation as established in the literature. Lastly, a direct comparison between the power ripple magnitude equation proposed in [16] and the experimental data is conducted.

The remainder of this work is organized as follows. In Section 2, the fundamental instantaneous characteristics of each power control strategy and their relationship to the unbalanced factor are analyzed. Section 3 presents a typical grid-connected converter control system structure. Section 4 details the experimental setup employed in this work. Section 5 presents and discusses the experimental results, and Section 6 states the main conclusions.

★

\*Corresponding author

 (); () (); ()

ORCID(s):

1

## 2. Pliant power control strategies

The analysis and results presented in this work rely on the following assumptions:

- The active and reactive power delivered at the PCC is constant in a grid voltage period;
- The inverter is connected through a three phase three wire system and thus there is no zero-sequence voltage and current component at the PCC;
- The system operates as an ideal grid-following converter so it can be modeled as a current controlled source;
- The instantaneous voltage sequence components are known and their absolute values are constant during the dip. Therefore, the unbalanced factor  $u = \frac{|V^-|}{|V^+|}$  is a scalar between 0 and 1;
- The phase angles of voltage and current sequences are constant during the sag

As stated in [14, p. 1], for any three-phase system, the instantaneous active and reactive power can be expressed, respectively, in terms of the scalar and cross-vector products of the instantaneous voltage and current column vectors:

$$p = \mathbf{v} \cdot \mathbf{i} \quad (1)$$

$$\mathbf{q} = \mathbf{v} \times \mathbf{i} \quad (2)$$

Consequently, the current vector  $\mathbf{i}$  can be decomposed into two mutually orthogonal components: the instantaneous active current vector ( $\mathbf{i}_p$ ) and the instantaneous reactive current vector ( $\mathbf{i}_q$ ). Using this definition,  $\mathbf{i}_q$  is orthogonal to  $\mathbf{v}$  (null dot product), whereas  $\mathbf{i}_p$  aligns with  $\mathbf{v}$  (null cross product). These properties imply in:

$$p = \underbrace{\mathbf{v}^+ \cdot \mathbf{i}_p^+}_{P^+} + \underbrace{\mathbf{v}^- \cdot \mathbf{i}_p^-}_{P^-} + \underbrace{\mathbf{v}^+ \cdot \mathbf{i}_q^+ + \mathbf{v}^- \cdot \mathbf{i}_q^-}_0 + \underbrace{\mathbf{v}^+ \cdot \mathbf{i}_p^- + \mathbf{v}^- \cdot \mathbf{i}_p^+}_{\tilde{p}} \quad (3)$$

$$q = \underbrace{|\mathbf{v}^+ \times \mathbf{i}_q^+|}_{Q^+} + \underbrace{|\mathbf{v}^- \times \mathbf{i}_q^-|}_{Q^-} + \underbrace{|\mathbf{v}^+ \times \mathbf{i}_p^+ + \mathbf{v}^- \times \mathbf{i}_p^-|}_0 + \underbrace{|\mathbf{v}^- \times \mathbf{i}_q^+ + \mathbf{v}^+ \times \mathbf{i}_q^- + \mathbf{v}^- \times \mathbf{i}_p^+ + \mathbf{v}^+ \times \mathbf{i}_p^-|}_{\tilde{q}} \quad (4)$$

As proposed by [19], the  $\tilde{p}$  and  $\tilde{q}$  compensation is achieved by applying a weighting coefficient  $k_{pq}$  to the products of the different voltage and current sequences vectors. Since  $\mathbf{i}_p^{+,-}$  is collinear to  $\mathbf{v}^{+,-}$ , there exist scalars  $\lambda^{+,-}$  such that:

$$\tilde{p} = \mathbf{v}^+ \cdot \mathbf{i}_p^- + \mathbf{v}^- \cdot \mathbf{i}_p^+ \quad (5)$$

$$\mathbf{v}^+ \cdot \mathbf{i}_p^- = k_p \mathbf{v}^- \cdot \mathbf{i}_p^+ \quad (6)$$

$$\mathbf{v}^+ \cdot (\lambda^- \mathbf{v}^-) = k_p \mathbf{v}^- \cdot (\lambda^+ \mathbf{v}^+) = \lambda^- = k_p \lambda^+ \quad (7)$$

An expression for  $i_p^-$  in function of  $k_p$  can be found isolating  $\lambda^+$  in  $P^+$  (eq. (3)):

$$\mathbf{v}^+ \cdot \mathbf{i}_p^+ = \mathbf{v}^+ \cdot (\lambda^+ \mathbf{v}^+) \longrightarrow \lambda^+ = \frac{\mathbf{v}^+ \cdot \mathbf{i}_p^+}{|\mathbf{v}^+|^2} \quad (8)$$

$$\mathbf{i}_p^- = \lambda^- \mathbf{v}^- = k_p \lambda^+ \mathbf{v}^- = \frac{k_p \mathbf{v}^+ \cdot \mathbf{i}_p^+}{|\mathbf{v}^+|^2} \mathbf{v}^- \quad (9)$$

Finally, substituting eq. (9) into the average power excerpt ( $P^+ + P^-$ ) in eq. (3) [18],  $i_p^{+,-}$  and thus  $i_p^*$  are obtained:

$$P|\mathbf{v}^+|^2 = (|\mathbf{v}^+|^2 + k_p |\mathbf{v}^-|^2)(\mathbf{v}^+ \cdot \mathbf{i}_p^+) \quad (10)$$

$$\mathbf{i}_p^+ = \frac{P}{|\mathbf{v}^+|^2 + k_p |\mathbf{v}^-|^2} \mathbf{v}^+ \quad (11)$$

$$\mathbf{i}_p^- = \frac{k_p P}{|\mathbf{v}^+|^2 + k_p |\mathbf{v}^-|^2} \mathbf{v}^- \quad (12)$$

$$\mathbf{i}_p^* = \frac{P^*}{|\mathbf{v}^+|^2 + k_p |\mathbf{v}^-|^2} (\mathbf{v}^+ + k_p \mathbf{v}^-) \quad (13)$$

A similar deduction exploiting the equivalent collinear property between  $\mathbf{i}_q^*$  and  $\mathbf{v}_\perp$  is presented in both articles, yielding:

$$\mathbf{i}^* = \frac{P^*}{|\mathbf{v}^+|^2 + k_p |\mathbf{v}^-|^2} (\mathbf{v}^+ + k_p \mathbf{v}^-) + \frac{Q^*}{|\mathbf{v}^+|^2 + k_q |\mathbf{v}^-|^2} (\mathbf{v}_\perp^+ + k_q \mathbf{v}_\perp^-) \quad (14)$$

Where  $\mathbf{v}_\perp$  is the voltage vector  $\mathbf{v}$  orthogonal projection. Subsequently,  $\mathbf{v}$  norm is given in time-domain as :

$$|v|^2 = |v^+|^2 + |v^-|^2 + 2|v^+||v^-| \cos(2\omega t + \phi^+ - \phi^-) \quad (15)$$

The instantaneous power oscillations in quadrature and in-phase [25] are accounted for replacing eq. (14) orthogonal components in eq. (3) and eq. (4), resulting in:

$$\tilde{p} = \left( \frac{(1 + k_p)|\mathbf{v}^+||\mathbf{v}^-| \cos(2\omega t + \phi^+ - \phi^-)}{|\mathbf{v}^+|^2 + k_p |\mathbf{v}^-|^2} \right) P^* + \left( \frac{(1 - k_q)|\mathbf{v}^+||\mathbf{v}^-| \sin(2\omega t + \phi^+ - \phi^-)}{|\mathbf{v}^+|^2 + k_q |\mathbf{v}^-|^2} \right) Q^* \quad (16)$$

$$\tilde{q} = \left( \frac{(1 + k_q)|\mathbf{v}^+||\mathbf{v}^-| \cos(2\omega t + \phi^+ - \phi^-)}{|\mathbf{v}^+|^2 + k_q |\mathbf{v}^-|^2} \right) Q^* - \left( \frac{(1 - k_p)|\mathbf{v}^+||\mathbf{v}^-| \sin(2\omega t + \phi^+ - \phi^-)}{|\mathbf{v}^+|^2 + k_p |\mathbf{v}^-|^2} \right) P^* \quad (17)$$

Rewriting  $\tilde{p}$  and  $\tilde{q}$  as a complex number, their magnitudes can be conveniently expressed as a function of the  $u$  unbalanced factor [16] and  $k_{pq}$  coefficients:

$$|\tilde{p}| = u \sqrt{\left(\frac{(1+k_p)P^*}{1+k_p u^2}\right)^2 + \left(\frac{(1-k_q)Q^*}{1+k_q u^2}\right)^2} \quad (18)$$

$$|\tilde{q}| = u \sqrt{\left(\frac{(1+k_q)Q^*}{1+k_q u^2}\right)^2 + \left(\frac{(1-k_p)P^*}{1+k_p u^2}\right)^2} \quad (19)$$

## 2.1. Non-sinusoidal current strategy

### 2.1.1. Instantaneous Active-Reactive Control

This strategy naturally arises from the generalized instantaneous reactive power theory (GIPT) geometric properties of  $\mathbf{i}_{pq}$ . Computing  $\mathbf{i}_p^*$  as orthogonal and  $\mathbf{i}_q^*$  as parallel vectors to  $\mathbf{v}$ , the IARC can effectively cancel power oscillations for any  $u$  and active/reactive references:

$$\mathbf{i}_p^* = \frac{P^*}{|\mathbf{v}|^2} \mathbf{v} \quad (20)$$

$$\mathbf{i}_q^* = \frac{Q^*}{|\mathbf{v}|^2} \mathbf{v}_\perp \quad (21)$$

However, as above equations states, its current references are proportional to  $|\mathbf{v}|^2$ . Since this norm is time-variant (eq. (15)) and directly linked to  $\mathbf{v}$  symmetric-sequence components norms, the resulting current reference is inherently non-sinusoidal. Furthermore, when only active power is delivered to the grid ( $Q^* = 0$ ), the total harmonic distortion (THD) of the current can be approximated as [26]:

$$\text{THD}_i = \frac{u}{\sqrt{1-u^2}} \quad (22)$$

This undesired harmonic content, which is heavily dependent on the unbalance factor, may not meet grid power quality requirements even for low ( $\geq 0.05$ )  $u$  values [27, p. 64].

## 2.2. Sinusoidal current strategies

### 2.2.1. Average Active-Reactive Control (AARC)

This strategy address the underlying problem present in the IARC: the second-order harmonics introduced by  $|\mathbf{v}|^2$  (eq. (15)). To counteract the cosine oscillation, the squared denominator in eq. (14) must enclose all the voltage sequence components delivered in one grid period i.e the RMS voltage:

$$\sqrt{|\mathbf{v}^+|^2 + k_{pq} |\mathbf{v}^-|^2} = \sqrt{\frac{1}{T} \int_0^T |\mathbf{v}|^2} \quad (23)$$

$$(24)$$

As a result,  $\mathbf{i}_{pq}$  are time-aligned with  $\mathbf{v}$  and  $\mathbf{v}_\perp$ , generating instantaneous power oscillations that are decoupled from each other's reference values. A important feature of this strategy is the lower conduction losses, whereas a drawback is necessary null reference to cancel  $\tilde{p}$  or  $\tilde{q}$ .

**Table 1**

Relationship between  $k_{pq}$  coefficients and the sinusoidal power control strategies

Strategy	$k_p$	$k_q$	$ p $	$ q $
AARC	1	1	$\frac{2u}{1+u^2} P^*$	$\frac{2u}{1+u^2} Q^*$
PNSC	-1	-1	$u \sqrt{(P^*)^2 + (Q^*)^2}$	$u \sqrt{(P^*)^2 + (Q^*)^2}$
BPSC	0	0	$\frac{2u}{1-u^2} Q^*$	$\frac{2u}{1-u^2} P^*$
APOC	-1	1	0	$u \sqrt{\left(\frac{2Q^*}{1+u^2}\right)^2 + \left(\frac{2P^*}{1-u^2}\right)^2}$
RPOC	1	-1	$u \sqrt{\left(\frac{2P^*}{1+u^2}\right)^2 + \left(\frac{2Q^*}{1-u^2}\right)^2}$	0

**Table 2**

Elaborated by the author.

### 2.2.2. Positive-Negative-Sequence Compensation (PNSC)

While the previous strategy tries to align the respective currents and voltages components respectively responsible for  $i_{p,q}$ , the PNSC introduces the negative sequence voltage vector as subtracted quantity, producing a complementary characteristic:  $\mathbf{i}$  orthogonal components are time-aligned to their opposing voltage orthogonal vectors. This weighting links  $\tilde{p}$  and  $\tilde{q}$  to their counterpart power reference aiming to cancel the oscillation when one of them is zero.

### 2.2.3. Balanced Positive-Sequence Control (BPSC)

In the Balanced Positive-Sequence Control strategy, only the positive-sequence voltage vector is employed to compute the reference currents. Since no negative-sequence component current is injected, both  $P^-$  and  $Q^-$  are zero, indicating that the average active and reactive power depend exclusively on  $P^+$  and  $Q^+$ , respectively. Nonetheless, as pointed in , the inner and cross products of  $\mathbf{i}_p^+$  and  $\mathbf{v}^-$  introduce power oscillations of equal magnitude in  $p$  and  $q$ , which are directly proportional to their respective reference values. Although these power oscillations are not eliminated for any reference value, this strategy is unique as it produces a perfectly balanced current set for any unbalance factor.

### 2.2.4. Active Power Oscillation Cancels (APOC)

As the  $\tilde{p}$  equation highlights, active power oscillation is a product of the inner product of  $\mathbf{v}^{+-}$  and  $\mathbf{i}^{+-}$ , which is exactly what APOC tries to compensate for alligning  $\mathbf{i}_p$  and  $\mathbf{v}_\perp$  maximums values. Thus, a constant  $p$  is obtained for whatever  $u$  factor and power references values. Nevertheless,  $\mathbf{i}_q$  is precisely collinear to  $\mathbf{v}$ , yielding the highest  $\tilde{q}$  possible.

### 2.2.5. Reactive Power Oscillation Cancels (RPOC)

A reciprocal approach to APOC is used in the Reactive Power Oscillation Cancels strategy, where  $\mathbf{i}_q$  is always perpendicular to  $\mathbf{v}_\perp$  objectiving a null cross product between them for arbitrary  $P^*$  and  $Q^*$  and unbalanced factor. Conversely, as predicted by IGPT, the second order oscillation superimposed on the active power will be at its peak.

### 3. System structure

#### 3.1. Converter topology

The schematic of the three-phase, three-wire grid-connected inverter analyzed in this study is illustrated in ???. The DC/DC stage consists of a three-level interleaved bidirectional half-bridge converter that manages battery power flow and controls active power delivery. This is followed by a two-level, three-phase inverter responsible for DC-link voltage regulation and current characteristics injected into the grid through an LCL filter. Both stages employ cascade control.

#### 3.2. Dc/ac control strategy

The inverter control strategy consists of two cascaded loops, being the faster inner-loop current control implemented in the  $\alpha\beta$  stationary reference frame (SRF) through an ideal proportional-resonant (PR) controller (eq. (25)) tuned at the fundamental frequency of the grid. The LCL capacitor dynamics are ignored and thus  $i_s$  is presumably equal to  $i_{abc}$ . The outer voltage loop acts as a reference for the current loop and control power flow (Grid service) by compensating the DC-link voltage. This voltage regulation is modeled using the square voltage method and achieved through a PI controller, as proposed in <ref>.

$$G_c(s) = K_p + K_r \frac{s}{s^2 + \omega_f^2} \quad (25)$$

##### 3.2.1. Sequence Detection

Accurate voltage sequence detection plays a crucial role in both reference current computation and grid synchronization. Therefore, a robust phase-locked loop (PLL) is essential. Considering that the current control is done in the SRF, the dual second order generalized topology (DSOGI-PNSC) arises as a convenient choice.

##### 3.2.2. Power control

### 4. Experimental setup

To assess the performance of the proposed power control strategies, experimental validation was conducted using the laboratory test setup shown in (??). The system consists of a battery energy storage system (BESS) interfaced with a programmable three-phase regenerative grid simulator (NHR 9410), which was configured to simulate a voltage sag in A and B phases. Although the  $pq$  theory states that, theoretically, no energy storage element is required to compensate for  $\tilde{p}$  and  $\tilde{q}$ , this particular setup is valuable for validating the ripple magnitude at the PCC, as it offers the following advantages:

- Battery storage fast responding dynamics as a constant dispatchable active power source
- The ability to maintain (ideally) zero active power exchange, as the batteries' discharge current counteracts the active power required for PCS operation.

**Table 3**

Parameters of the experimental system

PCS Parameters	Values
Dc/dc converter inductance	4 mH
Dc/dc converter switching frequency	9 kHz
Dc/ac stage switching frequency	9 kHz
Number of interleaved dc/dc converter cells	3
Grid and dc/ac stage side LCL filter inductance	1 mH
Capacitance of each module	4.7 mF
LCL filter capacitance	25 $\mu$ F
LCL filter damping resistance	1.8 $\Omega$
Grid voltage (RMS)	220 V
Grid frequency	60 Hz
Dc-link voltage	500 V
Nominal current (RMS)	16 A
Battery Parameters	Value
Rated Capacity (C/20)	36 A h
$V_{nom}$	12 V
$V_{boost}$	14.4 V
$V_{float}$	13.6 V
$R_{bat}$	7.2 $\Omega$
Maximum charge current	7.2 A

**Table 4**

Grid voltages, unbalanced factors and converter power references

$u$	$V_{a,b}$ V	$V_{a,b}$ [pu]
0.18	76.21	0.8
0.33	50.80	0.6
0.57	25.40	0.4
Converter Power References		
Active W	Reactive VAR	
0	1500	
1500	0	
1000	1000	

The instantaneous power waveforms were acquired at the DC/AC stage switching frequency using TMDSDOCK28379D development kits, which were employed to control the BESS power conversion system. The recorded data were then exported via Code Composer Studio to MATLAB for further analysis.

The key parameters of the case study are presented in table 3, while table 4 summarizes the selected unbalanced grid conditions and the active/reactive power reference values imposed on the converter for all  $u$  values.

### 5. Results



## References

- [1] IEA. *World Energy Outlook 2023*. International Energy Agency, 2023. URL <https://iea.blob.core.windows.net/assets/86ede39e-4436-42d7-ba2a-edf61467e070/WorldEnergyOutlook2023.pdf>.
- [2] IRENA. *Global energy transformation : a roadmap to 2050*. International Renewable Energy Agency, 2019. ISBN 9789292601218. URL [https://www.irena.org/-/media/Files/IRENA/Agency/Publication/2019/Apr/IRENA\\_Global\\_Energy\\_Transformation\\_2019.pdf](https://www.irena.org/-/media/Files/IRENA/Agency/Publication/2019/Apr/IRENA_Global_Energy_Transformation_2019.pdf).
- [3] IRENA. *Renewable capacity statistics 2024*. International Renewable Energy Agency, 2024. URL [https://www.irena.org/-/media/Files/IRENA/Agency/Publication/2024/Mar/IRENA\\_RE\\_Capacity\\_Statistics\\_2024.pdf](https://www.irena.org/-/media/Files/IRENA/Agency/Publication/2024/Mar/IRENA_RE_Capacity_Statistics_2024.pdf).
- [4] Haobo Zhang, Wang Xiang, Weixing Lin, and Jinyu Wen. Grid forming converters in renewable energy sources dominated power grid: Control strategy, stability, application, and challenges. *Journal of Modern Power Systems and Clean Energy*, 9(6):1239–1256, 2021. doi: <https://doi.org/10.35833/MPE.2021.000257>.
- [5] Thomas Ackermann, Thibault Prevost, Vijay Vittal, Andrew J. Roscoe, Julia Matevosyan, and Nicholas Miller. Paving the way: A future without inertia is closer than you think. *IEEE Power and Energy Magazine*, 15(6):61–69, 2017. doi: <https://doi.org/10.1109/MPE.2017.2729138>.
- [6] Amirhossein Sajadi, Jo Ann Rañola, Rick Wallace Kenyon, Bri-Mathias Hodge, and Barry Mather. Dynamics and stability of power systems with high shares of grid-following inverter-based resources: A tutorial. *IEEE Access*, 11:29591–29613, 2023. doi: <https://doi.org/10.1109/ACCESS.2023.3260778>.
- [7] Rafat Aljarrah, Bayan Bany Fawaz, Qusay Salem, Mazaher Karimi, Hesamoddin Marzoughi, and Rasoul Azizpanah-Abarghoee. Issues and challenges of grid-following converters interfacing renewable energy sources in low inertia systems: A review. *IEEE Access*, 12:5534–5561, 2024. doi: <https://doi.org/10.1109/ACCESS.2024.3349630>.
- [8] Ieee recommended practice for monitoring electric power quality. *IEEE Std 1159-2019 (Revision of IEEE Std 1159-2009)*, pages 1–98, 2019. doi: <https://doi.org/10.1109/IEEESTD.2019.8796486>.
- [9] Real-life power quality sags, 2017. URL <https://dx.doi.org/10.21227/H2K88D>.
- [10] IRENA. *Grid Codes for Renewable Powered Systems*. International Renewable Energy Agency, 2022. URL [https://www.irena.org/-/media/Files/IRENA/Agency/Publication/2022/Apr/IRENA\\_Grid\\_Codes\\_Renewable\\_Systems\\_2022.pdf](https://www.irena.org/-/media/Files/IRENA/Agency/Publication/2022/Apr/IRENA_Grid_Codes_Renewable_Systems_2022.pdf).
- [11] European Commission. Commission regulation (eu) 2016/631 of 14 april 2016 establishing a network code on requirements for grid connection of generators. Official Journal of the European Union, L 112, Apr 2016. pp. 1–68.
- [12] Claudionor F. Nascimento, Edson H. Watanabe, Oumar Diene, Alvaro B. Dietrich, Alessandro Goedtel, Johan J. C. Gyselinck, and Robson F. S. Dias. Analysis of noncharacteristic harmonics generated by voltage-source converters operating under unbalanced voltage. *IEEE Transactions on Power Delivery*, 32(2):951–961, 2017. doi: <https://doi.org/10.1109/TPWRD.2016.2593684>.
- [13] Holger Jedtberg, Marius Langwasser, Rongwu Zhu, Giampaolo Buticchi, Thomas Ebel, and Marco Liserre. Impacts of unbalanced grid voltages on lifetime of dc-link capacitors of back-to-back converters in wind turbines with doubly-fed induction generators. In *2017 IEEE Applied Power Electronics Conference and Exposition (APEC)*, pages 816–823, 2017. doi: <https://doi.org/10.1109/APEC.2017.7930790>.
- [14] Fang Zheng Peng and Jih-Sheng Lai. Generalized instantaneous reactive power theory for three-phase power systems. *IEEE Transactions on Instrumentation and Measurement*, 45(1):293–297, 1996. doi: <https://doi.org/10.1109/19.481350>.
- [15] Nagwa F. Ibrahim, Karar Mahmoud, Matti Lehtonen, and Mohamed M. F. Darwish. Comparative analysis of three-phase pv grid connected inverter current control schemes in unbalanced grid conditions. *IEEE Access*, 11:42204–42221, 2023. doi: <https://doi.org/10.1109/ACCESS.2023.3270262>.
- [16] Rafael M. Silva, Allan F. Cupertino, Guilherme M. Rezende, Clodualdo V. Sousa, and Victor F. Mendes. Power control strategies for grid connected converters applied to full-scale wind energy conversion systems during lvr operation. *Electric Power Systems Research*, 184: 106279, 2020. ISSN 0378-7796. doi: <https://doi.org/10.1016/j.epsr.2020.106279>. URL <https://www.sciencedirect.com/science/article/pii/S0378779620300857>.
- [17] Pedro Rodriguez, Adrian V. Timbus, Remus Teodorescu, Marco Liserre, and Frede Blaabjerg. Flexible active power control of distributed power generation systems during grid faults. *IEEE Transactions on Industrial Electronics*, 54(5):2583–2592, 2007. doi: <https://doi.org/10.1109/TIE.2007.899914>.
- [18] Fei Wang, Jorge L. Duarte, and Marcel A. M. Hendrix. Active power control strategies for inverter-based distributed power generation adapted to grid-fault ride-through requirements. In *2009 13th European Conference on Power Electronics and Applications*, pages 1–10, 2009.
- [19] Fei Wang, Jorge L. Duarte, and Marcel A. M. Hendrix. Pliant active and reactive power control for grid-interactive converters under unbalanced voltage dips. *IEEE Transactions on Power Electronics*, 26(5):1511–1521, 2011. doi: <https://doi.org/10.1109/TPEL.2010.2052289>.
- [20] Antonio Camacho, Miguel Castilla, Jaume Miret, Juan C. Vasquez, and Eduardo Alarcon-Gallo. Flexible voltage support control for three-phase distributed generation inverters under grid fault. *IEEE Transactions on Industrial Electronics*, 60(4):1429–1441, 2013. doi: <https://doi.org/10.1109/TIE.2012.2185016>.
- [21] Mohamed Azab. High performance decoupled active and reactive power control for three-phase grid-tied inverters using model predictive control. *Protection and Control of Modern Power Systems*, 6(3): 1–19, 2021. doi: <https://doi.org/10.1186/s41601-021-00204-z>.
- [22] Yajing Zhang, Jing Wang, Hong Li, Trillion Q. Zheng, Jih-Sheng Lai, Jianguo Li, Jiuhe Wang, and Qian Chen. Dynamic performance improving sliding-mode control-based feedback linearization for pv system under lvr condition. *IEEE Transactions on Power Electronics*, 35(11):11745–11757, 2020. doi: <https://doi.org/10.1109/TPEL.2020.2983315>.
- [23] Amir Sepehr, Oriol Gomis-Bellmunt, and Edris Pouresmaeil. Employing machine learning for enhancing transient stability of power synchronization control during fault conditions in weak grids. *IEEE Transactions on Smart Grid*, 13(3):2121–2131, 2022. doi: <https://doi.org/10.1109/TSG.2022.3148590>.
- [24] S. N. V. Bramaeswara Rao, Y. V. Pavan Kumar, Mohammad Amir, and Furkan Ahmad. An adaptive neuro-fuzzy control strategy for improved power quality in multi-microgrid clusters. *IEEE Access*, 10:128007–128021, 2022. doi: <https://doi.org/10.1109/ACCESS.2022.3226670>.
- [25] Xiong Du, Yue Wu, Shida Gu, Heng-Ming Tai, Pengju Sun, and Yongliang Ji. Power oscillation analysis and control of three-phase grid-connected voltage source converters under unbalanced grid faults. *IET Power Electronics*, 9(11):2162–2173, 2016. doi: <https://doi.org/10.1049/iet-pel.2015.0804>. URL <https://onlinelibrary.wiley.com/doi/abs/10.1049/iet-pel.2015.0804>.
- [26] Miguel Castilla, Jaume Miret, Jorge Luis Sosa, José Matas, and Luis García de Vicuña. Grid-fault control scheme for three-phase photovoltaic inverters with adjustable power quality characteristics. *IEEE Transactions on Power Electronics*, 25(12):2930–2940, 2010. doi: <https://doi.org/10.1109/TPEL.2010.2070081>.
- [27] Ieee standard for interconnection and interoperability of distributed energy resources with associated electric power systems interfaces. *IEEE Std 1547-2018 (Revision of IEEE Std 1547-2003)*, pages 1–138, 2018. doi: <https://doi.org/10.1109/IEEESTD.2018.8332112>.